External loads identification and shape sensing on an aluminum wing box: An integrated approach

External loads identification and shape sensing on an aluminum wing box: an integrated approach

Marco Esposito* [a,b], Marco Gherlone[b] and Pier Marzocca[a]

[a] Aerospace Engineering and Aviation, RMIT University, Melbourne, Australia

[b] Department of Mechanical and Aerospace Engineering, Politecnico di Torino, Torino, Italy

Abstract

The recent development of the Structural Health Monitoring (SHM) framework has required the simultaneous development of the tools fundamentals for its realization. The shape sensing methods and the loads identification ones have established themselves as crucial tools for the monitoring of aerospace structures. The two families of methods have been developed separately, although the possibility to achieve the knowledge of the displacement field and of the external loads together can enable a further progress in the SHM. In this paper, an integrated approach to simultaneously preform loads identification and shape sensing from discrete strain measurements is proposed. The methods is based on a two-steps process. The first step involves the identification of continuously distributed and concentrated external loads from discrete strain measurements. This step is achieved by discretizing the loads with Finite Elements (FE) and by computing the coefficients of influence between the nodal values of the loads and the discrete strain measurements. The second step reduces the shape sensing inverse problem to a simple direct Finite Element Analysis. The loads identified in the previous step are applied to a refined FE model of the structure and the displacement field is easily obtained through a direct FE analysis. This investigation proves that the two-steps method can accurately identify the loads and the displacement field of a wing box subject to an aerodynamic pressure distribution and a set of concentrated forces, when a sufficient number of strain information is available. When the number of discrete strain measurements decreases or the strains are affected by measurement error, the loads are poorly predicted but the method is still capable of an extremely accurate displacements reconstruction.

Keywords: Loads reconstruction; Shape sensing; Loads identification; Structural Health Monitoring; Wing box; Strain measurements

*Corresponding author.
Department of Mechanical and Aerospace Engineering, Corso Duca degli Abruzzi 24, 10129, Torino, Italy
e-mail: marco.esposito@polito.it

1 Introduction

Structural Health Monitoring (SHM) is witnessing a rapid development during the last decades and it is remarkably establishing itself as a key technology for the maintenance and design of modern aircraft. Within the SHM framework, two technologies have attracted considerable attention as crucial tools for the realization of an effective structural monitoring system: the external loads identification methods and the shape sensing methods. These two families of methods are designed to compute the external loads and the displacement field of a structure from discrete strain measurements. The monitoring of external loads and the shape sensing are a fundamental tool for the predictive maintenance operations of aerospace structures. The in-flight knowledge of the external loads could provide the in-flight load spectra, a fundamental input to the prediction models used for the estimation of the structure's remaining useful life [1]. Moreover, the monitoring of loads could supply information about the health status of the structures through the detection of changes in the load paths caused by presence of damages [2]. The same approach can be used for the shape sensing. As proven in [3, 4], it is possible to detect damages in a structure by finding anomalies in the displacement and strain fields trough shape sensing. Differences in the strain signals from damaged and undamaged helicopter blades have also been used for the same purpose in [5]. Furthermore, the knowledge of the in-flight load conditions and displacements is fundamental for the design of innovative smart structures that, thanks to their morphing capabilities, could optimize their shape to obtain load alleviation [6] and to improve the aerodynamic efficiency of the control surfaces [7]. In addition, structures that carry antennas could improve the performance of their communication systems using the deformation data to improve their on-orbit shape estimation.

The constant progress of these techniques has been pushed by the simultaneous improvement achieved in the field of the strain sensing technology. The development of strain sensing systems based on optical fibers has allowed the easy and reliable sensing of a large numbers of discrete strains, that were not conceivable with the traditional strain gauges. Recently, the use of fiber optics distributed strain sensing systems [8, 9] has further increase the amount of information that can be provided to the aforementioned strain-based methods.

The loads identification research is mainly focused on the reconstruction of the pressure distribution resulting from a continuously distributed aerodynamic load. Shkarayev *et al.* [10] developed a method based on the parametric approximation of the aerodynamic loading. This method requires the formulation of the unknown pressure distribution as a linear combination of known pressure distributions multiplied by unknown coefficients. The coefficients are computed by studying the strain fields caused by each known pressure distribution and by fitting, in a least-square sense, the linear combination of these strain fields to the discrete measured strains. The method proved to be really accurate on the identification of two pressure distributions on a rectangular wing box, but it requires the a priori definition of a pressure distribution function as close as possible to the actually applied one. Following the same approach, Cameron *et al.* extended the method by adopting single Fourier cosine terms [11] and double Fourier series [12] to parameterize different two-variables pressure distributions over a square plate.

In [13], Airoldi *et al.* parameterized the complex external loads acting on a composite spar with a set of

concentrated loads. They used a least-square approach to identify the parameterized load set from discrete strains. They also used the reconstructed load to carry on a direct FEM analysis for the evaluation of the strain and of the displacement field. The study proved that, also in the case where the parameterized loads were poorly identified, the strain field could be accurately reconstructed. The main focus of the paper was on the accuracy of the reconstructed strains distribution and on how the strain sensors could be distributed on the structure.

In [1], Nakamura *et al.* proposed a pressure distribution identification technique based on the discretization of the pressure field with Finite Elements. Triangular elements are used to discretize the spatial domain of flat wing-shaped plate, where the pressure is applied. The pressure field is interpolated from its unknown nodal values using spatial shape functions. The unknown nodal values of the pressure are computed by fitting the strain field caused by each nodal value of the pressure to the discrete measured strains. This method does not need any a priori knowledge of the form of the unknown pressure distribution. In fact, when the method has been compared to a Neural Network based approach in [14], it has proven to be more effective when the unknown pressure form was different from the ones that the network was trained with. Neural Networks were also successfully adopted for the prediction of discrete external loads applied on the vertical tail of the F/A-18 [15] and on a wing rib [16].

Different families of shape sensing methods have been developed and widely applied on a large number of structural problems: methods based on the numerical integration of the strain measurements and the Bernoulli-Euler beam theory [17–19], methods based on the use of the modal shapes and the modal strain shapes [20–22] and method based on an inverse formulation of the Finite Element Method (FEM). A detailed review of the existing shape sensing methods can be found in [23]. The inverse Finite Element Method (iFEM), firstly developed in [24], has emerged as one of the most promising and widespread shape sensing method in literature. It is based on the finite element discretization of a structural domain and on the consequent formulation of the strain field in terms of the nodal values of the displacements and of the derivatives of the element's shape functions. The unknowns of the problem, the nodal displacements, are computed minimizing the error between the strains expressed in terms of the nodal displacements and the actually measured strains. The method has been successfully applied to beams and truss structures [25,26] and to flat, curved and thin walled plates [27–32]. In particular, in [33] it has been compared with other shape sensing methods and has proven to be the most accurate in the reconstruction of the deformed shape of a composite wing box.

In this work, a two-steps integrated approach for the simultaneous identification of the external loads and of the displacement field from discrete strain measurements is proposed and numerically implemented on a 3D aluminum swept wing box. The first step concerns the computation of the external loads. The proposed procedure extends the method introduced in [1] with the use of quadratic elements for the computation of the pressure field. Moreover, a load case consisting of concentrated forces is also considered as in [13]. The second step focuses on the reconstruction of the displacement field induced by the two load cases. Thanks to the proposed procedure, the shape sensing is reduced to a simple direct problem. The identified external loads are applied to a detailed FE model of the wing box and, by performing a standard direct FEM analysis,

the displacement field is easily computed. The results of the shape sensing step are compared with the ones obtained with the iFEM. A study on the influence of the number of measured strains and of measurement error on the accuracy of the integrated approach is also performed. The two-step approach is based on the work by Airoldi et al. [13] while introducing some novelties: (i) the load identification step is extended to distributed loads and (ii) a more detailed accuracy investigation is performed on the reconstructed displacement field. The two-steps method is able to accurately identify the external loads and the relative deformed shape of the wing box when a sufficient amount of strain information is available. When the number of strain measurements decreases the method loses accuracy in the identification of the loads, but it is still capable of an impressive accuracy in the in the reconstruction of the deformed shape. The method is capable of remarkable accuracy in the reconstruction of the displacement field when measurement error is present, if the Tikhonov regularization is adopted to smooth the ill-posedness of the problem.

The paper is structured as follows. In Section 2 the load identification method adopted in this paper is described. In Section 3 the proposed two-steps approach for the shape sensing is introduced in detail. In Section 4 the case study is described and the wing box and the simulation models are introduced. The load cases and the induced deformed shapes, object of the reconstructions, are also presented. In Section 5 the two-steps procedure, as adopted in this work, and the final results are presented and commentated. Finally, the concluding remarks are discussed in Section 6.

2 External loads identification

The load identification method firstly developed by Nakamura *et al.* [1] is able to reconstruct the pressure continuously distributed on a x-y plane from discrete strain measurements. The method is based on the interpolation of the pressure distribution through finite elements. As for the classical FEM, the structural domain, where the pressure is applied, is discretized using Finite Elements. Within the element, the pressure distribution is interpolated from the nodal values of the pressure using shape functions. Mathematically, it can be formulated as follows:

$$p^e(x,y) = \sum_{i=1}^{n} N_i^e(x,y)\ p_i^e \tag{1}$$

where $p^e(x,y)$ is the pressure distribution over the element's x-y plane, $N_i^e(x,y)$ are the shape functions dependent from the chosen element formulation, n is the number of nodes of the element and p_i^e are the nodal values of the pressure.

If the domain is discretized with a mesh of pressure elements, the global $N_i(x,y)$ shape functions, related to the global m_p nodes of the pressure mesh, can be computed by means of the assembly procedure adopted by the standard FEM. Consequently, the pressure distribution over the entire domain, $p(x,y)$, can be expressed as

follows:

$$p(x,y) = \sum_{i=1}^{m_p} N_i(x,y)\ p_i \tag{2}$$

where p_i is the nodal value in the i-th node of the mesh.

Therefore, in analogy with the classical structural FEM problem, in this case, the degrees of freedom (DOFs) of the system, that represents the unknowns of the problem, are the nodal values of the pressure, p_i. Once these values are computed, the full pressure distribution can be derived using an interpolation through the selected shape functions.

Since the objective of the method is to reconstruct the pressure distribution from discrete strain measurements, it is necessary to find a relation between the discrete strain measurements and the unknown nodal values of the pressure. If the hypothesis of linear elasticity is considered, the j-th measured strain component, ε_j^m, can be expressed as the superposition of the ε_{ji}^m strains induced by the m_p nodal pressures, p_i. Moreover, in the linear elastic regime, the i-th strain contribution, ε_{ji}^m, induced by the i-th p_i will be linearly proportional to the i-th nodal pressure itself. These considerations lead to the following formulation of the j-th strain component:

$$\varepsilon_j^m = \sum_{i=1}^{m_p} \varepsilon_{ji}^m = \sum_{i=1}^{m_p} s_{ji}\ p_i \tag{3}$$

where s_{ji} is the i-th unknown coefficient of linear combination that relates the j-th strain component to the i-th nodal values of the pressure. When m_s measured strain components are available, the Eq. 3, expressed in matrix form, becomes:

$$\{\varepsilon^m\}_{m_s \times 1} = [s]_{m_s \times m_p} \{p\}_{m_p \times 1} \tag{4}$$

The matrix $[s]_{m_s \times m_p}$ can be easily computed through the iterative resolution of a direct FE problem. The i-th column of the matrix is computed by imposing that $p_i = 1$ and $p_k = 0$ $(k \neq i)$ in Eq. 2. The resulting pressure field is then applied to a FE model of the structure and the desired strain components are measured. Iterating the procedure to the m_p columns, allows the computation of the entire matrix. The application of this procedure requires the construction of an accurate FE model of the structure. Therefore, the geometry, the material properties and the constraints of the structure have to be known. No constraints need to be imposed on the relative positioning of the elements and nodes of the pressure mesh and of the refined one. More in general, the two meshes' characteristics can be very different from each other, as long as they share the discretization of one portion or of the entire structural domain. It is only necessary to be able to map the locations of the nodes, belonging to the refined mesh, to the elements of the pressure mesh, in order to compute the values of the pressure at these locations. The practical application of this procedure will be described in details in

Section 5.1.

Once the $[s]$ matrix is built, the expression of the nodal pressures as a function of the measured strain is easily obtained by inverting Eq. 4. Since in practical applications $m_s \neq m_p$, the inversion of $[s]$ is obtained by means of Moore-Penrose pseudo inverse matrix formulation, $[s^+]$:

$$\{p\} = [s^+]\{\varepsilon^m\} \tag{5}$$

By substituting the actually measured values of the strains into $\{\varepsilon^m\}$, the expression gives the nodal values of the pressure that best fit the actually applied pressure distribution that induced the measured strains. These nodal values of the pressure can then be used to reconstruct the full pressure field by substituting them into Eq. 2.

The same principles can be adopted for the identification of concentrated loads. In this case, the formulation does not need an interpolation of the nodal values of the load within the elements. The investigated loads are concentrated at a given location, therefore, they do not need to be expanded to any spacial domain. In the same linear elastic conditions assumed before, the j-th strain component, ε_j^m, induced by the i-th concentrated load, F_i, is linearly proportional to the load value. Moreover, if m_f concentrated forces are present, the strain component can be expressed as a superposition of the strains induced by each concentrated load. In analogy to Eq. 4, the vector of measured strains, can be expressed as follows:

$$\{\varepsilon^m\}_{m_s \times 1} = [s_f]_{m_s \times m_f}\{F\}_{m_f \times 1} \tag{6}$$

where $[s_f]_{m_s \times m_f}$ is the matrix of the coefficients of influence between the strains and the concentrated loads. The i-th column of the matrix is computed by imposing that $F_i = 1$ and $F_k = 0$ $(k \neq i)$ and measuring the induced m_s strain components. The pseudo-inversion of $[s_f]$ allows the computation of the vector of the concentrated forces that induced the actually measured strains:

$$\{F\} = [s_f^+]\{\varepsilon^m\} \tag{7}$$

3 Shape sensing

Shape sensing is a family of methods that allow the reconstruction of the displacement field from discrete strain measurements. In this section, a novel methodology that exploits the load identification as a tool for the shape sensing, is introduced.

In structural analysis, the direct problem aims to compute the displacement field, and from it the stress and strain field of a structure, when the structure's geometry, material properties, constraints and external

loads are known. The direct problem is usually solved by the application of the FEM. It is mathematically well-conditioned, that is, small perturbations in the inputs produce small perturbations in the outputs [34]. On the other hand, the shape sensing and the external loads identification are inverse problems and are often more difficult to solve. They are mathematically ill-posed and small perturbations in the inputs generally produce greater perturbations in the outputs [34]. In the previous section, a solution for the loads identification inverse problem has been presented. The objective of the proposed method is to use the results of the loads identification for the formulation of the shape sensing problem so that it could be reduced to a direct structural problem. By doing this, the resolution of only one inverse problem leads to the easy resolution of the other.

The method is based on a two step process. In the first step, the inverse problem of inferring the external load from discrete strain measurements is solved with the method described in Section 2. As highlighted before, this step requires the construction of a detailed FE model. Once the external loads are computed, in the second step, they can be applied to the detailed FE model to perform a direct structural analysis and thus used to compute the full displacement field of the structure, easily solving the shape sensing problem. This method allows the integration of the two structural health monitoring tools in a unique procedure, as illustrated in the scheme in Fig. 1, where the fist step is depicted in green color and the second step is depicted in orange color. Although the procedure can appear complex and computationally expensive, it is not and the real-time computation of the loads and the displacement field can be achieved by the method. In fact, once the models and the sensors configuration are established, the computationally expensive procedures, such as the computation of the $[s^+]$ or $[s_f^+]$ and the inversion of the stiffness matrix ($[K]$), relative to the direct FEM problem, are performed only one time and do not vary if the components of the vector of measured strains ($\{\varepsilon^m\}$) change. Therefore, every different vector of measured strains is simply multiplied by $[s^+]$ or $[s_f^+]$ to derive $\{p\}$ or $\{F\}$, that are, in turn, multiplied by $[K^{-1}]$ to compute the displacements. In practice, the whole procedure of computing the loads and the displacements is reduced to two simple and fast to compute matrices multiplications.

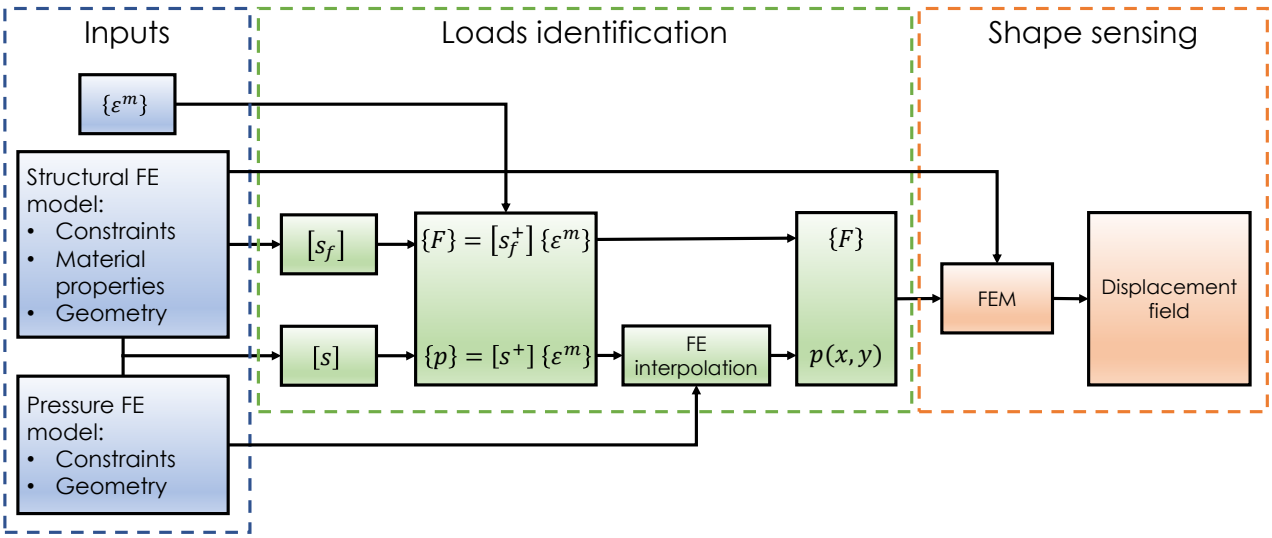

Figure 1: Loads identification and shape sensing integrated process - The inputs of the process are highlighted in blue. The load identification step is highlighted in green and the shape sensing step is highlighted in orange.

Besides the proposed method, several shape sensing techniques have been studied and compared in literature. These include the inverse Finite Element Method, that has emerged as one of the most promising one. Moreover, in [33], it has been proven that the method is particularly suitable, when compared to other methods, for the shape sensing of a wing box. Therefore, in this work, the iFEM is used as the reference shape sensing method to evaluate and compare the accuracy of the proposed approach. The detailed iFEM formulation adopted throughout the paper is the same described in [33].

4 Case study

The scope of this work is to identify the external loads and the displacement field of a wing box. In the following section the geometry, the materials, the load cases and the numerical models that define the analyzed wing box are presented.

4.1 Geometry and materials

The wing box object of the study is illustrated in Figure 2. The box is composed of two swept panels. The panels are connected to the two spars by four stiffeners and are reinforced by two stringers, one on each panel. Overall, the entire wing box is divided into seven bays by six rectangular ribs plus the tip section's one. The four stiffeners and the two stringers have a constant section along the wing span. The detailed geometry of each component is described in Figure 2. The root section of the wing box is clamped. In Figure 2, the reference coordinate frame, identified by the axis x,y and z, is also illustrated.

The wing box components are made of two different Aluminum alloys. The panels, the spars and the ribs are made of a 7075 Aluminum alloy, while the stiffeners and the stringers are made of a 6060 Aluminum alloy. The mechanical properties of the two alloys are presented in Table 1.

Table 1: Aluminum alloys mechanical properties.

Alloy	E $[GPa]$	ν	G $[GPa]$
6060	66	0.33	24.8
7075	72	0.32	27.2

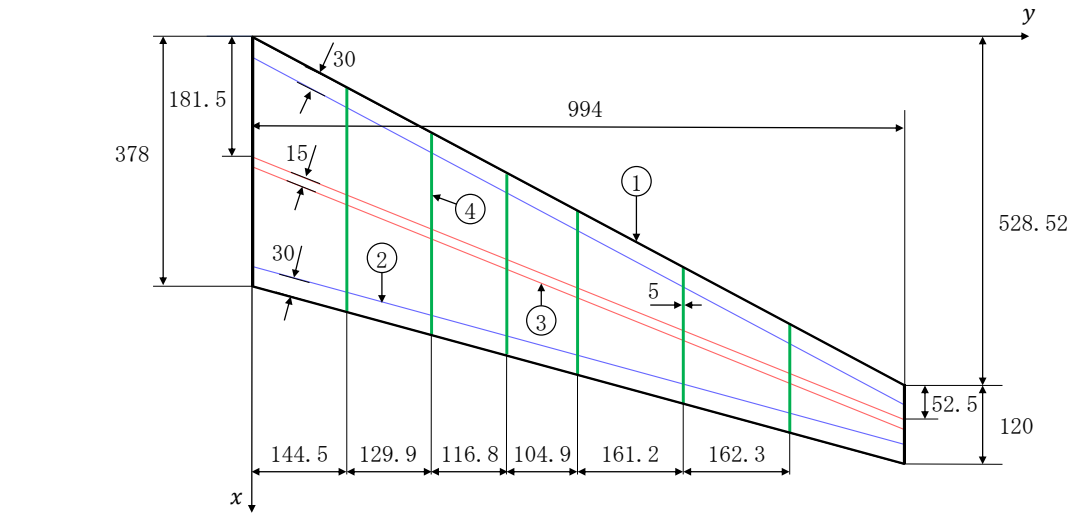

(a) top view

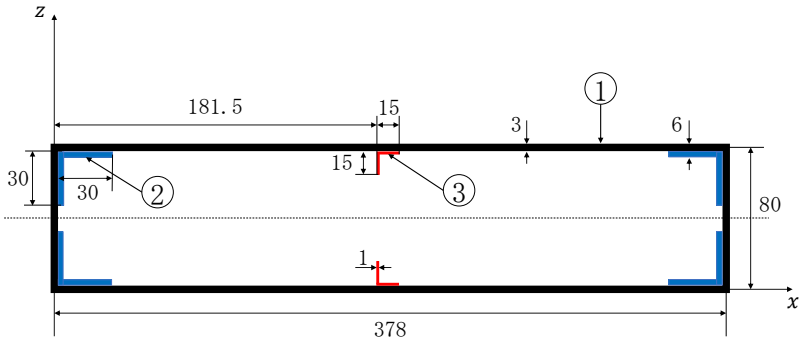

(b) root section ($y = 0$)

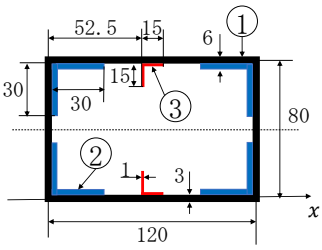

(c) tip section ($y = 994$)

Figure 2: Wing box geometry - In the figure, the panel and the spars are indicated by ①, the stiffeners that connect the skin panels to the spars are indicated by ②, the stringers are indicated by ③ and the ribs are indicated by ④. All dimensions are expressed in $[mm]$.

4.2 Load cases

This study focuses on the identification of the external loads and the displacements induced by them on the previously described wing box. In particular, two load cases and the relative deformed shapes, are investigated. These load cases have been chosen in order to cover the two kinds of loads whose identification process has been described in Section 2. Therefore, the first load case (Load Case 1) is constituted by a pressure distribution, intended to simulate an aerodynamic pressure distribution, and the second one (Load Case 2) by a set of concentrated forces, intended to simulate the presence of a pod on the wing tip.

The considered pressure distribution has been applied on the upper panel of the box and can be observed in Figure 3. The distribution is a multiplication of a cubic polynomial function of x and a quadratic one of y. The structural domain, where the distribution is defined, and the relative x and y coordinates are illustrated in Figure 2a. The chosen distribution is aimed to be representative of an aerodynamic pressure that, along the wing span direction, has a maximum at the root section and vanishes at the tip section. Along the chord direction, it vanishes at the leading and treadling edge and has a maximum at one-third of the chord. As a

consequence, mathematically, the polynomial function of y is constructed imposing that the function vanishes at the tip section, it has a maximum at the root section and this maximum is equal to 1. The cubic polynomial of x is defined by imposing that it vanishes at the trailing and leading edges, it has a maximum at one third of the chord and this maximum is equal to 1. The mathematical expression of the pressure distribution $p(x, y)$ and of the aforementioned conditions can be found in Appendix A. The deformed shape of the wing box, when subjected to the pressure distribution, is reported in Figure 4.

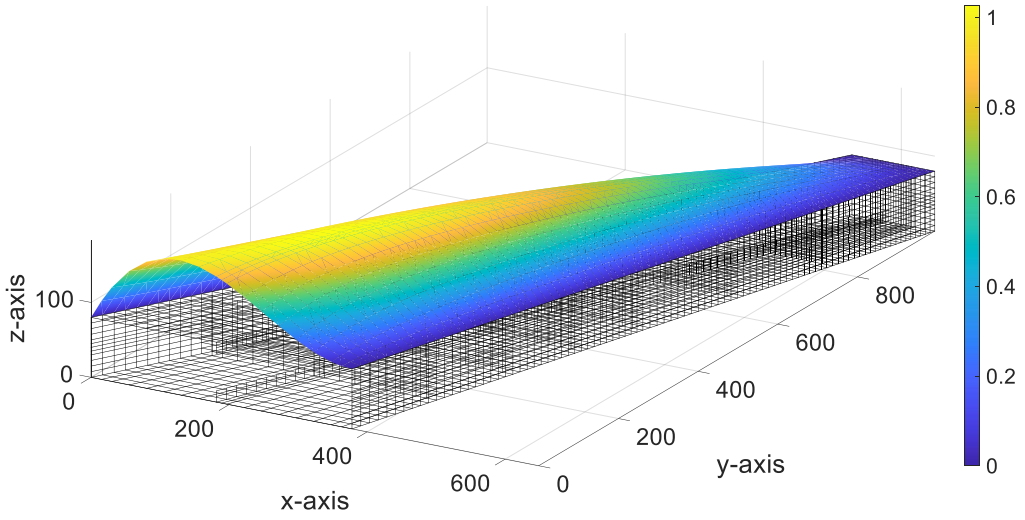

Figure 3: Load Case 1 on the refined FE model - The figure shows the pressure distribution applied on the refined FE model of the wing box. The pressure is expressed in $[N/mm^2]$

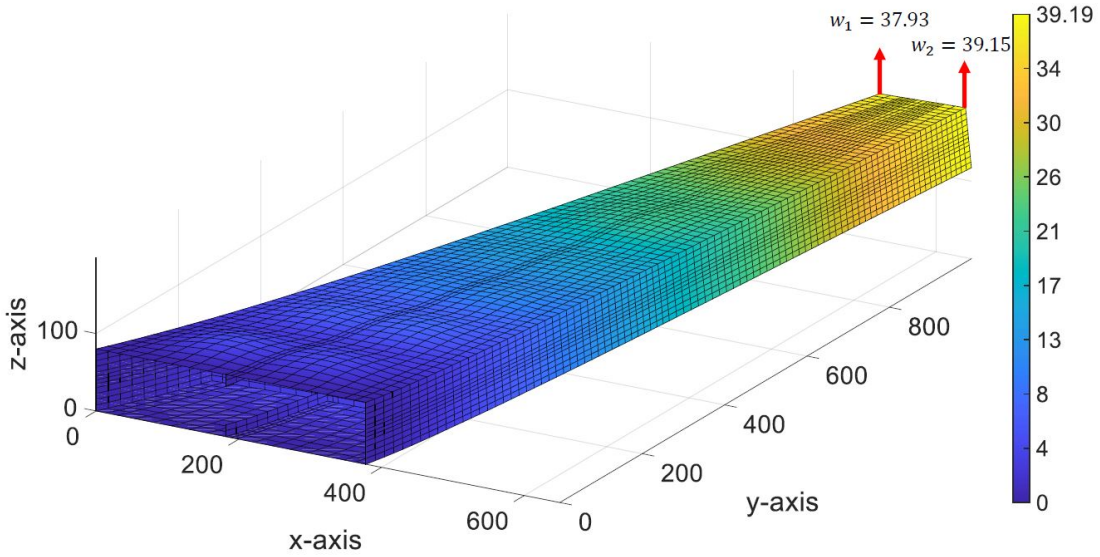

Figure 4: Deformed shape for the Load Case 1 - The figure shows the refined Fe model of the wing box deformed under the pressure distribution of the Load Case 1. The color bar refers to the magnitude (in mm) of the resultant displacements.

The second load case (Load Case 2) is constituted by a distributed load applied on the upper side of the tip rib. The load distribution is constant along the chord, is directed along the negative direction of z and has a constant value of 100 N/mm. This Load Case is designed to simulate the presence of a pod mounted on the wing tip. The discretization of this load in a finite element model is obtained by reducing the distributed load to concentrated forces applied in the nodes. The finite element representation of the distributed load, by means of nodal forces, is illustrated in Figure 5. These nodal forces represents the unknowns of the load identification problem for the second load case. The wing box, deformed under the loads of the second load case, is presented in Figure 6.

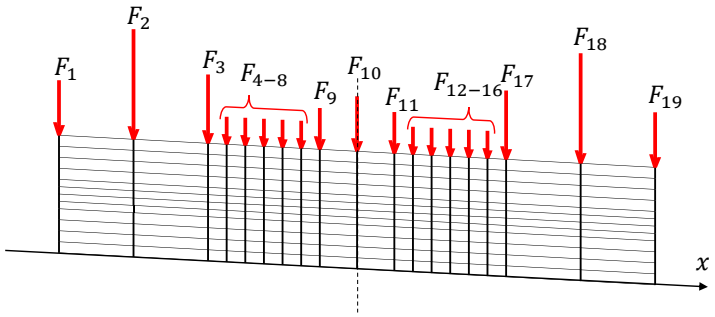

Figure 5: Load Case 2 - The figure shows the distributed load applied on the wing tip section, discretized to nodal forces according to the FEM. The value of the nodal forces are reported in Table 2.

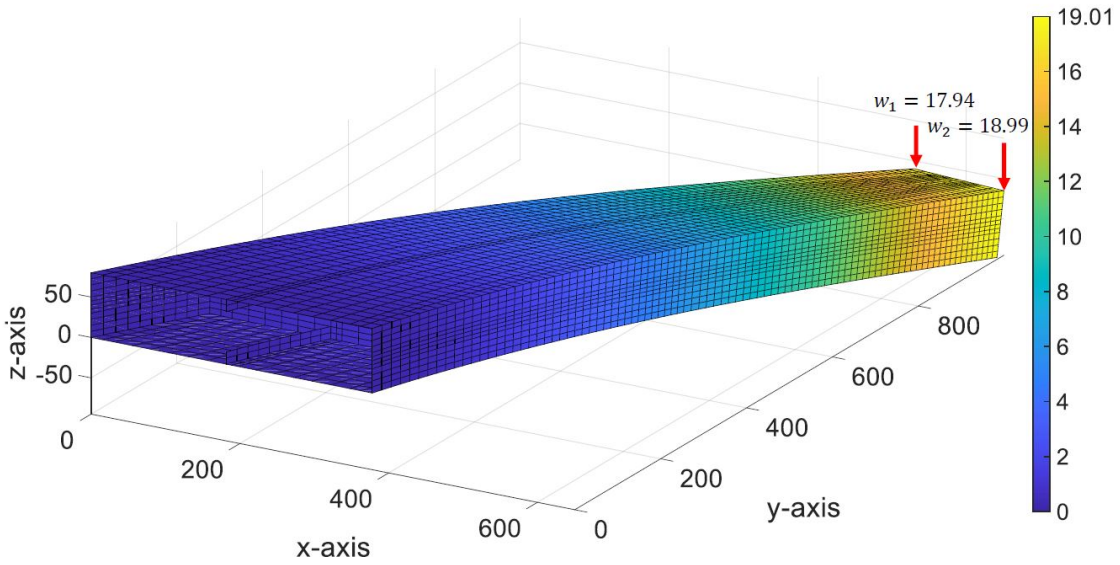

Figure 6: Deformed shape for the Load Case 2 - The figure shows the refined FE model of the wing box deformed under the distributed load of the Load Case 2. The color bar refers to the magnitude (in mm) of the resultant displacements.

In conclusion, the two load cases, object of the load identification in the next sections, are summarized in Table 2 and the deformed shapes, object of the shape sensing investigation, are reported in Figures 4 and 6.

Table 2: Load Cases.

Load Case	Loads	Constraints
Load case 1	$p(x,y) = (a_x x^3 + b_x x^2 + c_x x + d_x) \cdot (a_y y^2 + b_y y + c_y)$	Clamped root section
Load case 2	$F_1 = F_{19} = 749N;\ F_2 = F_{18} = 1,499N;\ F_3 = F_{17} = 937N;$ $F_{4-8} = F_{12-16} = 375N;\ F_9 = F_{11} = 562N;\ F_{10} = 749N$	Clamped root section

4.3 Models

The application of the load identification method and of the novel shape sensing technique requires the definition of a detailed FE model of the structure. Moreover, since the nature of this study is numerical, this model will be also used to simulate the real behavior of the wing box and, consequently, used to generate the input strains for the application of the methods and the reference displacements for the evaluation of the accuracy of the shape sensing. The refined model is the one that appears in the Figures 3, 4 and 6. It is presented in details in Figure 7b. It is constituted of 9,792 CQUAD4 NASTRAN® elements and of 7,129 nodes.

For the definition of the discrete pressure field, a coarser mesh to interpolate the nodal values of the pressure and the definition of the elements' formulation for the pressure discretization is needed. In the previous section, the pressure field of the Load Case 1 has been described. It is applied on the top panel of the box. Since the pressure is only defined there, the domain that needs to be discretized for the interpolation of the pressure is only the upper panel of the wing box. Differently from the previous application [1], where triangular elements were selected, in this case, the pressure field is discretized using quadrilateral elements. Within each quadrilateral element, the pressure is interpolated from its four nodal values using the standard bilinear shape functions, as described in [35]. It means that in Eq. 1 $n = 4$ and $N_i^e = (1+\chi_i\chi)(1+\eta_i\eta)$, where χ and η are the quadrilateral isoparametric coordinates and the subscript i denotes the computation relative to the i-th node. The pressure mesh is composed of 405 so formulated quad elements and of 460 nodes. It is illustrated in Figure 7a, where only the upper panel mesh, shown in red, is the one relative to the pressure.

A third model is also necessary for the application of the iFEM that is used as a benchmark for the evaluation of the accuracy of the shape sensing. The inverse FE mesh is illustrated in red and black in Figure 7a. For simplicity, the iFEM mesh is constructed so that the upper panel discretization is the same used for the pressure mesh. The model is built with 1818 iQS4 quadrilateral elements, whose formulation is the one adopted in [33]. This formulation requires the attribution of the strain measurements to the centroid of the elements. Consequently, the model is made so that the centroid of each inverse element has a correspondent node in the detailed structural FE model. This allows the easy attribution of the strains coming from the detailed model to the centroids of the iQS4 elements.

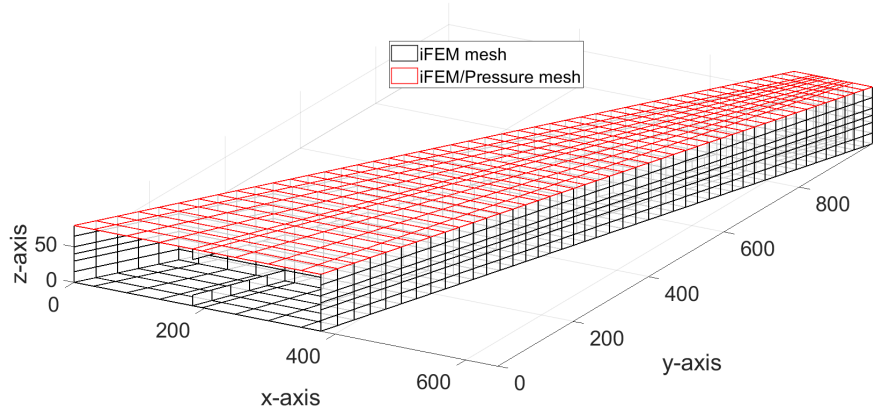

(a) iFEM/Pressure mesh

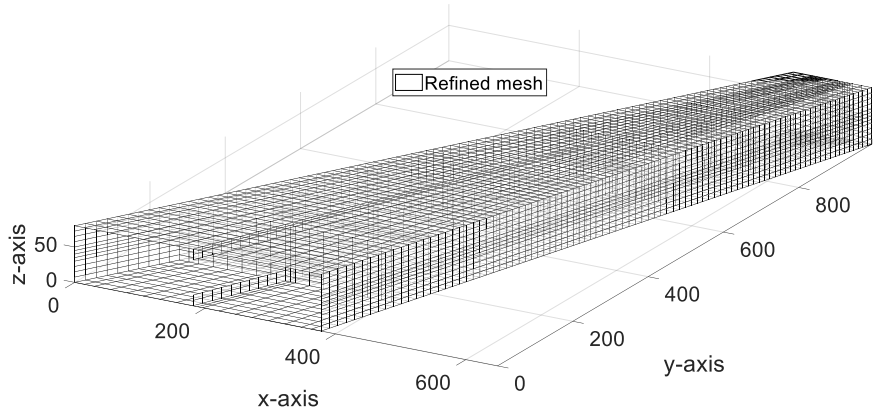

(b) Refined mesh

Figure 7: Models - In panel a, the elements whose contours are shown in red belong to the iFEM mesh and the pressure mesh. The elements whose contours are shown in black belong to the iFEM mesh only. In panel b, the refined mesh is presented.

5 Numerical simulations

In the following, the novelties introduced in this work, represented by the use of the quadrilateral elements for the pressure mesh and by the novel two-steps procedure for the computation of the displacements of the structure, are implemented on the numerical analysis of the test case described in Section 4. The detailed description of the procedure and of the evaluation criteria is provided. The influence of the sensors configuration on the accuracy of the new method is also presented in the following.

5.1 Matrices computation

The two-steps procedure begins with the computation of the $[s]$ and $[s_f]$ matrices, necessary for the application of the load identification step. In this work, a detailed study on the influence of the sensors configurations has been considered and will be described in Section 5.2. To compute the matrices mentioned above it is necessary to define all the possible locations and strain components that can be selected to create the specific sensors configurations that will be effectively used in the application of the method. The possible strains configurations chosen for this application have been inspired by the use of strain sensing systems based on optical fibers. This technology is in continuous development and it is establishing itself as one of the most effective for SHM applications. Consequently, the eligible strain measurements positions are located along lines running from the root section to the tip section and passing through the centroid of the iFEM mesh's elements. That allows the easy application of this method and, as mentioned before, the easy computation of the strains from the refined FE model, since these locations have a correspondent node in the model. According to the sensing possibilities of the optical-fiber-based sensors, the strains are measured along the sensing lines' directions. The sensing lines are distributed over the box as illustrated in Figure 8. As it is shown, 9 sensing line for each panel and 6 for each spar are selected, accounting for a total of 30 lines. For each line 45 measurement location are considered. A total of 1,350 strain components along the sensing lines represent the space of the possible strain components. All the considered strain components are measured on the external surface of the box. This implies that, for the iFEM formulation, the measured strain is considered constant through the thickness of the shell element.

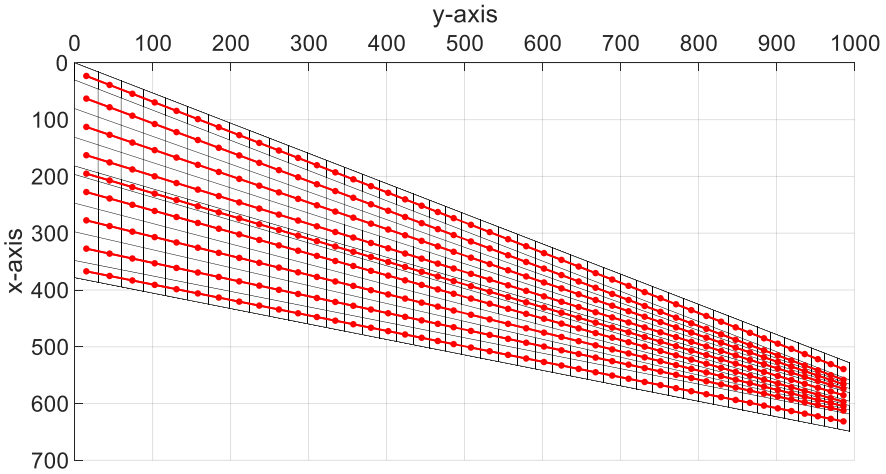

(a) Upper/Lower panels

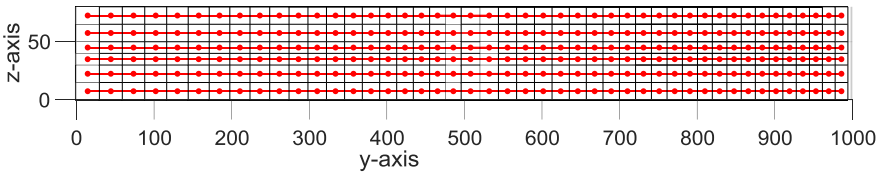

(b) Front/Rear spar

Figure 8: Sensing lines - In the figure, the sensing lines are showed only for one panel and one spar. The same configurations should be considered for the other components.

Once the space of the measured strains is defined, it is easy to compute the $[s]$ and $[s_f]$ matrices. The i-th

column of the $[s]$ matrix is computed by imposing that the p relative to the i-th node of the pressure mesh is equal to 1 and the other ones are equal to 0. The pressure field, interpolated through the shape functions, can be evaluated in every point of the pressure elements that pertain to the i-th node. In particular, it is necessary to compute the pressure values at the points, within the elements, where nodes of the refined FE model are located. This can be done by mapping these nodes to the elements' natural coordinates [36] and by computing the values of the pressures at these locations. The obtained nodal values of the pressure are then applied to the refined FE model and the induced 1,350 selected strains are computed. This process has to be repeated for all the 460 nodes of the pressure mesh, thus obtaining a $1,350 \times 460$ matrix. The same procedure can be adopted for the computation of the $[s_f]$ matrix. The only difference is that the unit load for the computation of the i-th column of the matrix does not have to be expanded to the whole domain and it can be directly applied to the i-th node of the refined model. In this case, since 19 unknown vertical forces are present, the $[s_f]$ is a $1,350 \times 19$ matrix.

5.2 Sensors optimization

Selecting the strain measurements that are actually used as an input to compute the external loads is translated mathematically in selecting the rows of the $[s]$ or $[s_f]$ matrix that correspond to the measured strain components. The substitution of the measured strains components into ε^m in Eqs. 5 and 7 completes the process. The procedure, as described here, allows the fast computation of the external loads for different strain sensors configurations. In fact, the computationally expensive procedure of populating the matrices is only performed once.

In this paper, the influence of the number of strain measurements on the accuracy of the loads identification and the shape sensing technique is investigated. Therefore, the effect of selecting a different number of sensing lines from the ones depicted in Figure 8 is studied. For each load case, 10 configurations with a varying number of sensing lines increased from 1 to 10 are considered, i.e. the configuration 1 considers 1 sensing line, the configuration 2 considers 2 sensing lines and so on. This implies that the $[s]$ and $[s_f]$ matrices are constituted of a varying number of rows, according to the number of selected lines. Therefore the two matrices present the following structure $[45, 450] \times 460$ and $[45, 450] \times 19$ respectively, with the number of rows varying from 45 to 450.

Each configuration is optimized so that the accuracy of the external load identification is the best that can be obtained with the correspondent finite number of sensing lines. More in details, the optimization is obtained by means of a Genetic Algorithm whose objective is to minimize the root mean square percent error ($\%ERMS$) between the computed nodal value of the load and the actually applied one. The expression of the $\%ERMS$ for a generic quantity, g, is:

$$\%ERMS_g = 100 \times \sqrt{\frac{1}{k}\sum_{i=1}^{k}\left(\frac{g_i - g_i^{ref}}{g_{max}^{ref}}\right)^2} \tag{8}$$

where k is the number of nodes where the quantity is computed, g_i is the reconstructed quantity in the i-th node, g_i^{ref} is the reference value of the quantity in the i-th node and g_{max}^{ref} is the maximum value of the reference quantity. For the optimization of Load case 1 $g = p$, on the other hand, for Load case 2, $g = F$.

The optimization generates 10 optimal sensors configurations and the respective 10 identified external loads for each load case. These identified loads are used, in the second step of the process (Figure 1), as the external loads to be applied on the refined FE model to obtain the deformed shape of the wing box through direct FEM analysis. The accuracy of this shape sensing results is evaluated with the same expression in Eq. 8 using $g = w$, where w is the displacement along the z axis. This displacement is chosen because it is the most relevant in the wing box deformation.

The sensors configurations are also optimized for the iFEM, in order to compare the novel shape sensing method with the best results from the chosen reference one. The exactly same approach is used and 10 optimized sensors configurations are obtained using a Genetic algorithm having as objective the minimization of the $\%ERMS_w$. The optimization for the two-steps approach and for the iFEM are carried on separately. Therefore, the optimal sensors configurations may be different for each method.

5.3 Results

5.3.1 From Tria to Quad

The first step of the analysis has been the evaluation of the accuracy in the pressure field reconstruction of the introduced quadrilateral element. Therefore, the reconstruction of the pressure field from the Load case 1, discretized with the quad mesh illustrated in Figure 7a, has been compared with the reconstruction of the pressure field, discretized using four triangular meshes, with varying characteristics in terms of the number of DOFs and of the regularity of the mesh.

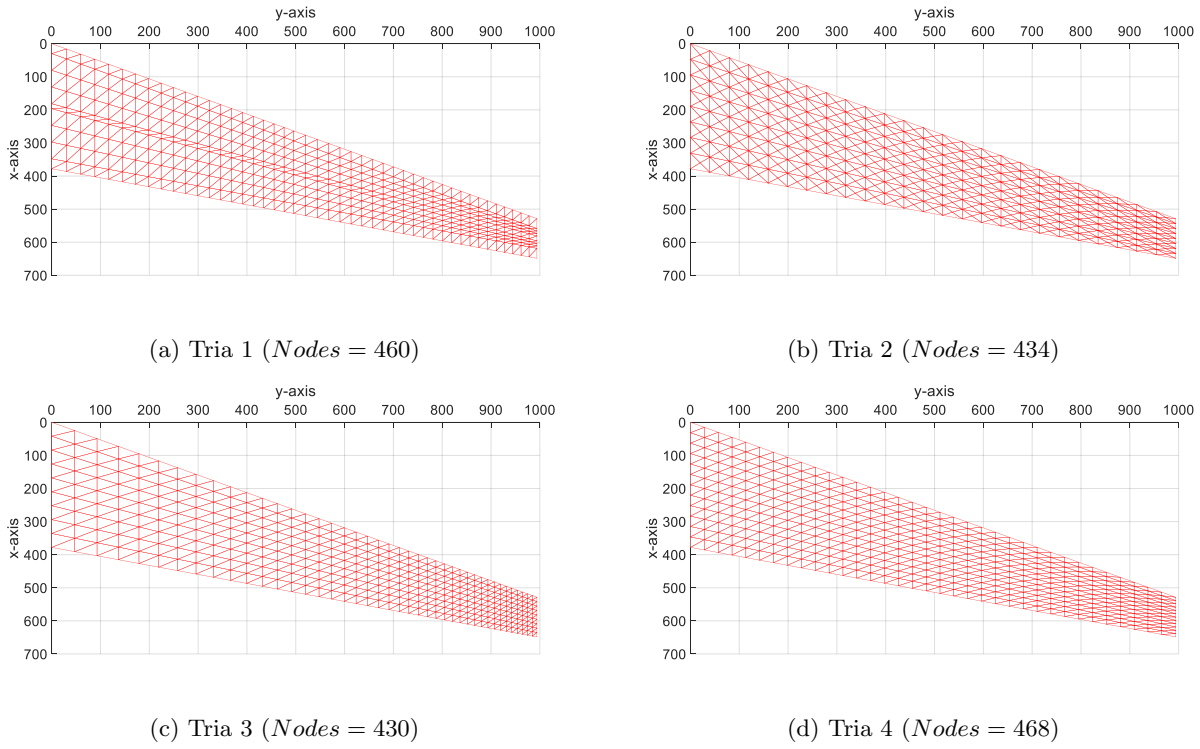

(a) Tria 1 ($Nodes = 460$)

(b) Tria 2 ($Nodes = 434$)

(c) Tria 3 ($Nodes = 430$)

(d) Tria 4 ($Nodes = 468$)

Figure 9: Triangular meshes - In the figure are illustrated the four triangular meshes used to evaluate the accuracy of the newly introduced quad element.

The **Tria 1** mesh, showed in Figure 9a, has been obtained splitting the elements of the quad mesh along one diagonal and, consequently, presents the same number of nodes and unknown nodal values of the pressure (460) of the quad mesh. The **Tria 2** mesh (Figure 9b), on the other hand, has been constructed splitting the quadrilateral elements of a different mesh along both diagonals. It has a slightly lower number of nodes (434). Finally, the **Tria 3** (Figure 9c) and **Tria 4** (Figure 9d) meshes are obtained by meshing the structural domain with a varying number of elements. In this phase, the whole set of $1,350$ axial strain sensors described in Section 5.1 has been used in order to compare the absolute accuracy, not influenced by the sensors configuration.

Table 3: Quadrilateral and triangular meshes comparison .

Mesh	#nodes	$\%ERMS_p$	%Diff
Quad	460	0.732	-
Tria 1	460	0.768	+4.9%
Tria 2	434	2.564	+250.3%
Tria 3	430	0.984	+34.4%
Tria 4	464	1.021	+39.5%

In Table 3, the $\%ERMS_p$ obtained using the full set of axial strains and the four different meshes are reported. The values of the $\%ERMS_p$ show that the introduction of the quadrilateral elements is able to reduce the error, and consequently increase the accuracy, by 4.9% with respect to the triangular mesh with the same number of DOFs and a similar meshing scheme. Moreover, the results obtained for **Tria 2**, **Tria 3** and **Tria 4** show that the introduction of different meshing schemes and different numbers of DOFs does not allow the triangular

elements to reach the accuracy of the quadrilateral ones, on the contrary, it exhibits a negative effect.

5.3.2 Load Case 1

The results of the sensors optimization for the reconstruction of the pressure distribution of the Load case 1 are reported in Figure 10. The 10 optimized sensors configurations, obtained for a varying number of sensing lines from 1 to 10, are shown. Using only one sensing line, a value of 16.05% of the $\%ERMS_p$ is obtained. This value decreases rapidly when increasing the number of lines from 2 to 7 where it reaches a value of 1.65%. A further increase in the amount of strain information provided to the method does not result in a significant increase in the accuracy of the reconstruction. In fact, the best result, obtained with 10 sensing lines, is slightly better than the one obtained with 7, giving an $\%ERMS_p$ value of 1.24%. The same trend in the accuracy of the reconstructions can be observed in Figure 12 and 13. Figure 12 shows the reconstructed pressure field for the optimized sensors configurations with 1 and 7 sensing lines. The comparison of the reconstructions with the reference pressure distribution (Figure 3) reveals the different level of accuracy reached with the two configurations. The more detailed analysis in Figure 13 shows the reconstruction of the pressure along the wing span for the sensors configurations with 1, 3, 5 and 7 sensing lines. The reconstructions are obtained along the line of nodes, from the pressure mesh, closest to points located at one-third of the chords.

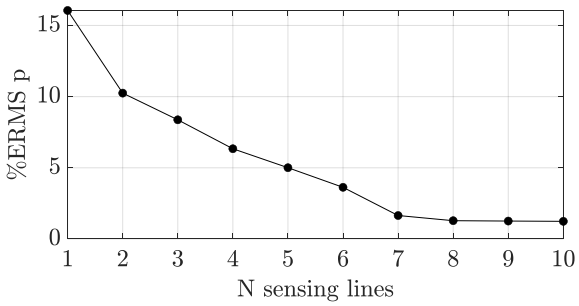

Figure 10: Pressure field reconstruction of Load Case 1 - The $\%ERMS_p$ for the best sensors configuration, with the number of sensing lines varying from 1 to 10, are reported.

The shape sensing step is obtained applying the reconstructed pressure fields to the refined FE model and by performing a standard FEM analysis. The $\%ERMS_w$ obtained for this shape sensing step are shown in Figure 11a. They can be compared with the results obtained by the iFEM on the same problem. In Figure 11b, the $\%ERMS_w$, obtained with the iFEM for the 10 optimized sensors configurations, are reported. The comparison points out the extreme level of accuracy of the two-steps method. Although the two methods show the same trend with respect to the variation in the number of sensing lines, the two-steps method is able to reach an $\%ERMS_w$ that is, in the worst case, equal to 0.19% and in the best one $2.64 \times 10^{-4}\%$. The iFEM's best result, on the other hand, is worst than every two-steps' one, reaching a minimum $\%ERMS_w$ value of 6.61%. The maximum one, considering only one sensing line, is equal to 38.80%. In addition, these results are supported by Figure 14. The figure shows the reconstructed deflection along the same line of nodes adopted in Figure 13. The deflections, obtained with the iFEM and with the two-steps method, are compared with the reference

vertical displacements obtained by the refined FE analysis. The iFEM results are reported for the configuration with 10 sensing line, whereas for the two-steps method the results are reported for the configurations with 1, 3, 5, and 7 lines. Nonetheless, the deflections of the two-steps method are superimposed to the reference one for every sensors configurations and are significantly more accurate than the iFEM one. Only the configuration with 1 sensing line presents a slight deviation from the reference close to the root section of the wing.

It is important to notice that the two-steps procedure is able to accurately reconstruct the deformed shape of the wing box even when the pressure field is not accurately reconstructed. The configuration with only one sensing line shows a considerable discrepancy between the reconstructed pressure field and the actually applied one (Figures 12a and 13a). Nevertheless, the method is able of an accurate shape sensing also with only one sensing line. This aspect will be examined more in deep when analyzing the results of the second load case.

In Figure 15, the optimal sensors configuration for the two-steps method, using 7 sensing lines, and for the iFEM, using 10 sensing lines, are reported. The configurations show that the optimization selected only sensors on the panels for the two-steps method, whereas only sensors on the spars for the iFEM.

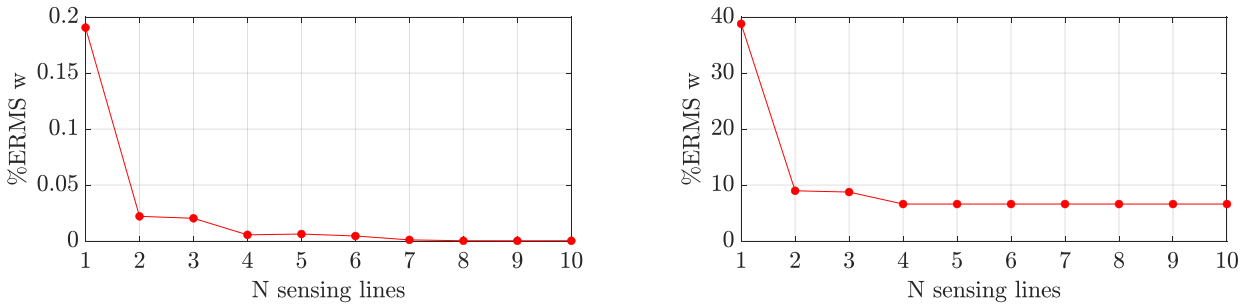

(a) Two-steps shape sensing results

(b) iFEM shape sensing results

Figure 11: Shape sensing for Load Case 1 - The $\%ERMS_w$ for the best sensors configuration, with the number of sensing lines varying from 1 to 10, are reported for the two-steps method (a) and the iFEM (b).

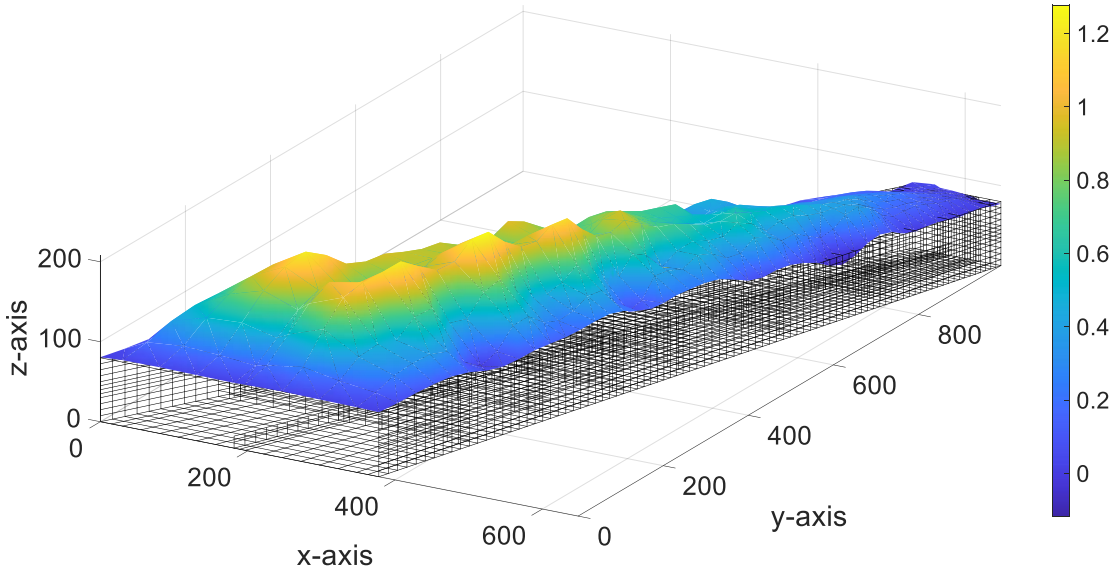

(a) 1 sensing line

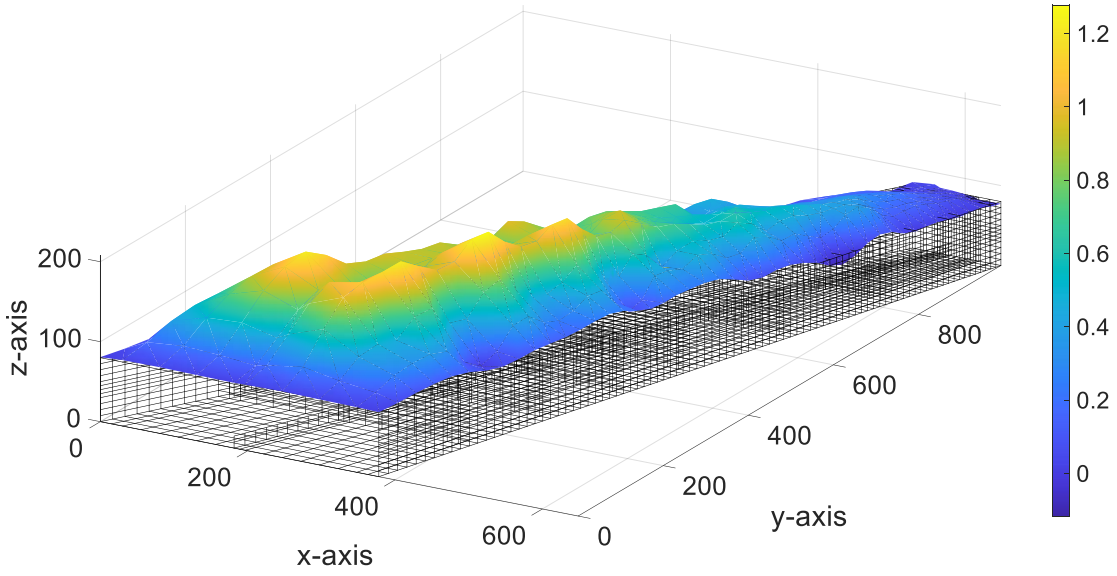

(b) 7 sensing lines

Figure 12: Pressure field reconstructions for Load Case 1.

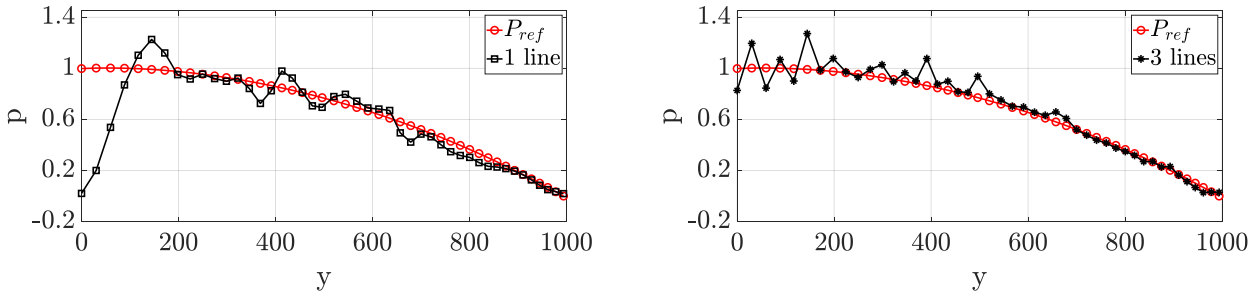

(a) 1 sensing line

(b) 3 sensing lines

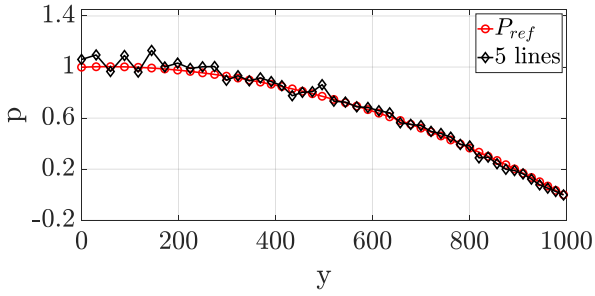

(c) 5 sensing lines

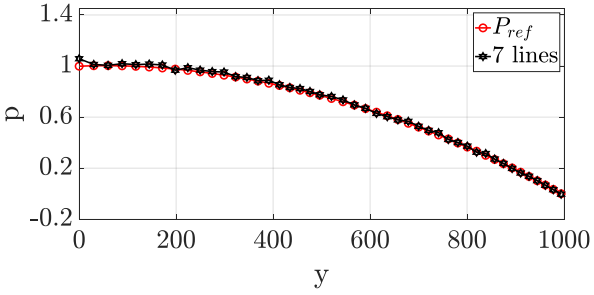

(d) 7 sensing lines

Figure 13: Pressure reconstruction along the wing span for Load Case 1.

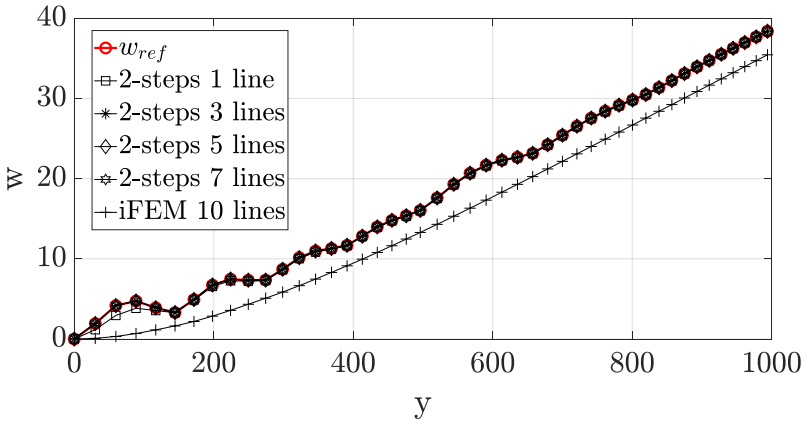

Figure 14: Vertical deflection along the wing span for Load Case 1.

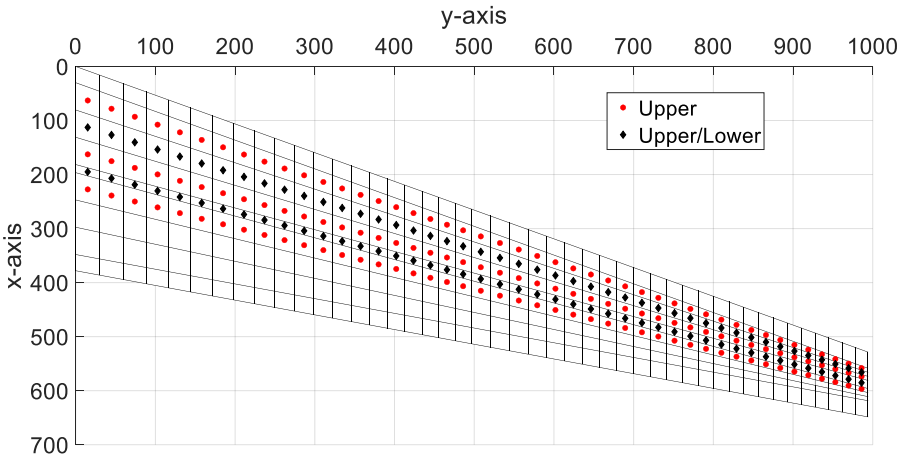

(a) two-steps method.

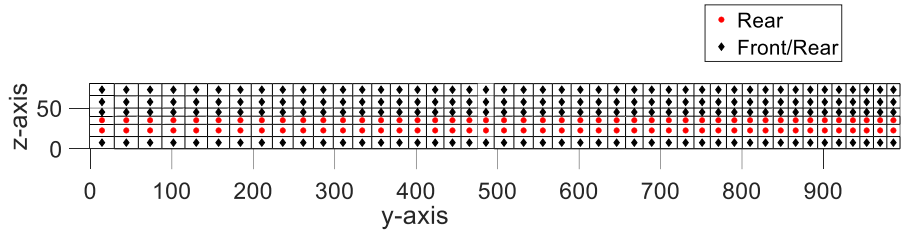

(b) iFEM

Figure 15: Optimal sensors configurations for Load case 1 - The figures show the optimal sensors configurations for the two-steps method (a) and the iFEM (b). In the legends, Upper and Lower refer to sensors located on the upper or lower panel, whereas Upper/lower refers to sensors located on both panels. Front and Rear refers to sensors that are located on the front or the rear spar, whereas Front/Rear refers to sensors located on both spars.

5.3.3 Load Case 2

The results of the identification of the nodal forces of the Load Case 2 are reported in Figure 16. The $\%ERMS_f$ has a worst maximum value of 50.10%, when only one line of sensors is available. If the number of sensing lines is increased to 2, the result does not improve, therefore the same result of the previous configuration is considered as the best. Improving the number of lines from 3 to 10 continuously improves the accuracy of the forces identification, reaching a significant precision for 7 ($\%ERMS_f = 0.49\%$), 8 ($\%ERMS_f = 0.11\%$), 9 ($\%ERMS_f = 0.060\%$) and 10 ($\%ERMS_f = 0.034\%$) lines of sensors. The identification of the nodal values of the force for the configurations with 1, 3, 5 and 7 sensing lines along the wing tip chord are reported in Figure 18.

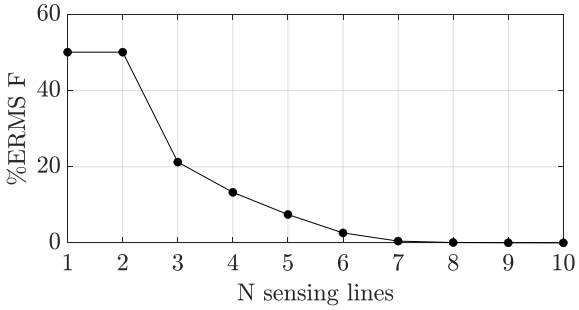

Figure 16: Nodal forces identification of Load Case 2 - The $\%ERMS_p$ for the best sensors configuration, with the number of sensing lines varying from 1 to 10, are reported.

The shape sensing step, in this case, is performed applying the identified values of the nodal forces to the refined model of the wing box. The results, in terms of the $\%ERMS_w$ and the number of optimized sensing lines, are illustrated in Figure 17a. The application of the iFEM to the deformation of this load case produces the values of the $\%ERMS_w$ reported in Figure 17b. In this application, the iFEM proves to be more accurate than in the previous load case. Nonetheless, the two-steps approach also shows more accurate predictions of the vertical displacements. Therefore, as for the previous load case, also for this one, the novel approach is consistently more precise and it achieves impressive results also for the case with only one sensing line. The iFEM is capable of reaching an $\%ERMS_w$ of 2.75% selecting 4 sensing lines. Increasing the number of lines does not give beneficial effects on the overall shape reconstruction. Consequently, the 4 lines configuration has been considered the best also for the configurations with more senors. When reducing the number of strain information, the iFEM still shows acceptable capabilities for the 2 lines configuration, where the $\%ERMS_w$ value is 4.10%. A further reduction in the number of strains causes a considerable rise in the value of the error, that reaches 31.5%. The two-steps technique sees a constant decreasing in the quality of the shape sensing with the decrease in the number of sensing lines too. Nevertheless, the values of the $\%ERMS_w$ are comprised between 4.13×10^{-6}%, when 10 line are selected, and 0.015%, when 1 line is selected, thus resulting in an impressive accuracy for all the sensors configurations. The impressive accuracy can be noted in Figure 19 as well. The vertical displacements along the wing tip chord of the reference solution are reported together with the one reconstructed with the two-steps method and with the iFEM. There is no visible deviation of the two-steps solutions from the reference one for the four different sensors configurations, with 1, 3, 5 and 7 sensing lines. On the other hand, the iFEM results, using 4 sensing lines, show an almost constant offset in the reconstruction of the vertical displacement along the chord.

In Figure 20, the optimal sensors configurations for the two-steps method, using 7 sensing lines and for the iFEM, using 4 sensing lines, are illustrated. Also in this case, it can be noticed that the optimizer tended to select sensors on the panels for the two-steps approach, with only one line selected on the rear spar and all the remaining lines selected on the upper panel. This case confirmed, on the other hand, the selection of sensors located only on the spars for the iFEM.

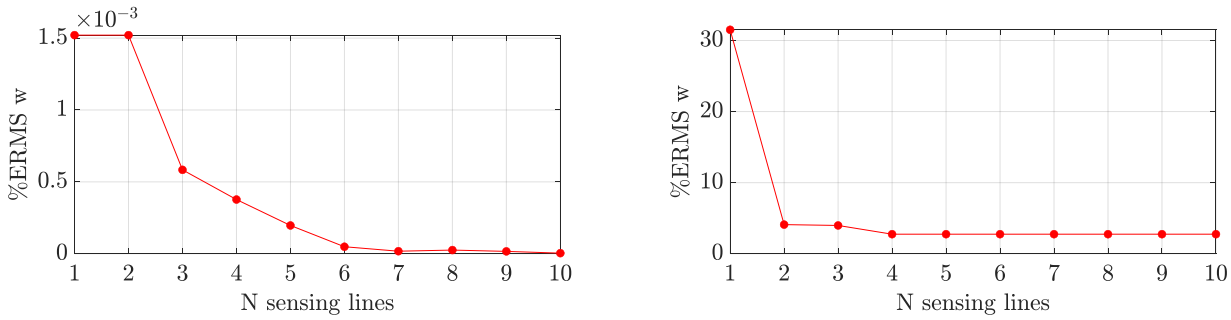

(a) Two-steps shape sensing results

(b) iFEM shape sensing results

Figure 17: Shape sensing for Load Case 2 - The $\%ERMS_w$ for the best sensors configuration, with the number of sensing lines varying from 1 to 10, are reported for the two-steps method (a) and the iFEM (b).

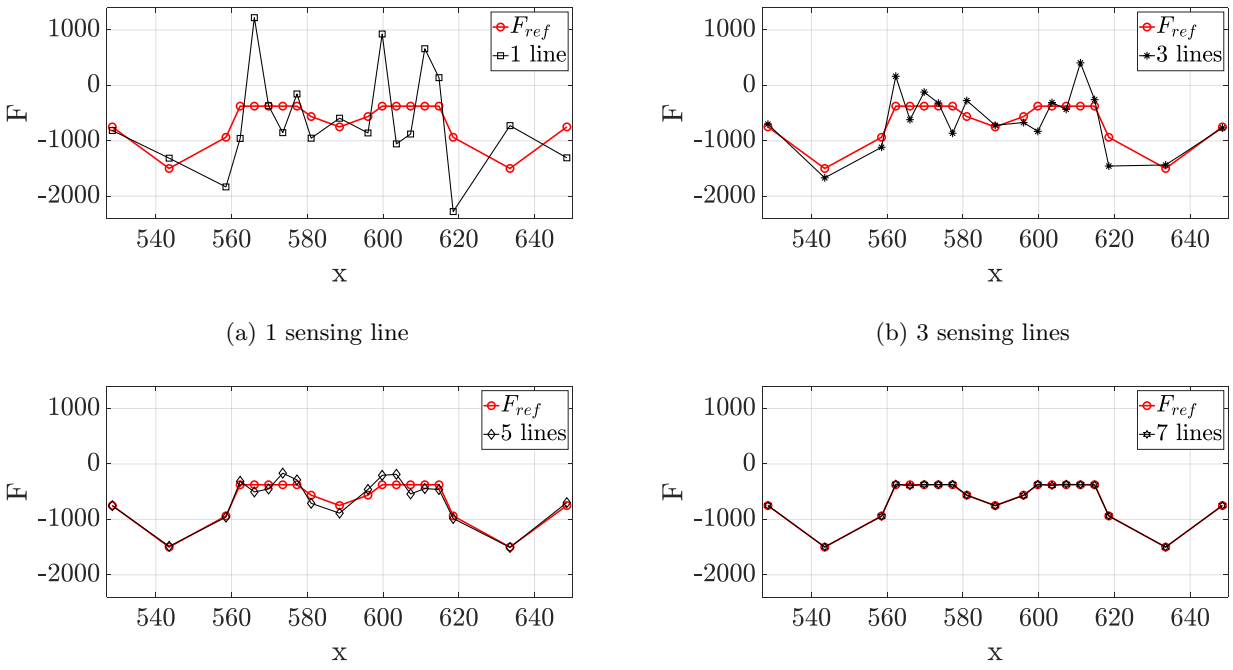

(a) 1 sensing line

(b) 3 sensing lines

(c) 5 sensing lines

(d) 7 sensing lines

Figure 18: Nodal forces identification along the wing tip chord for Load Case 2.

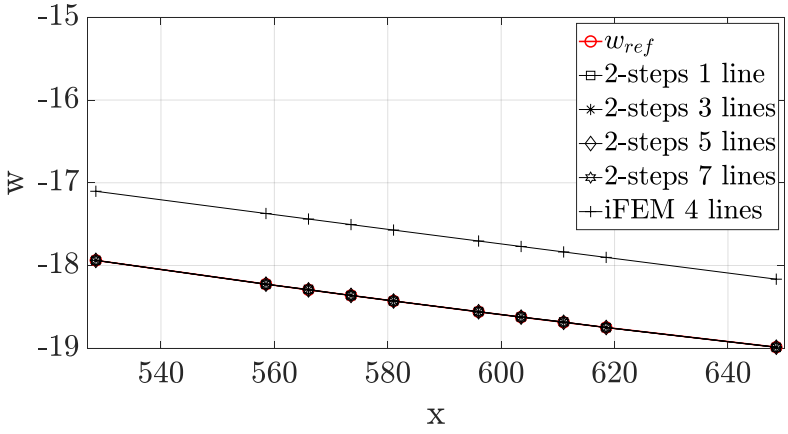

Figure 19: Vertical deflection along the wing tip chord for Load Case 2.

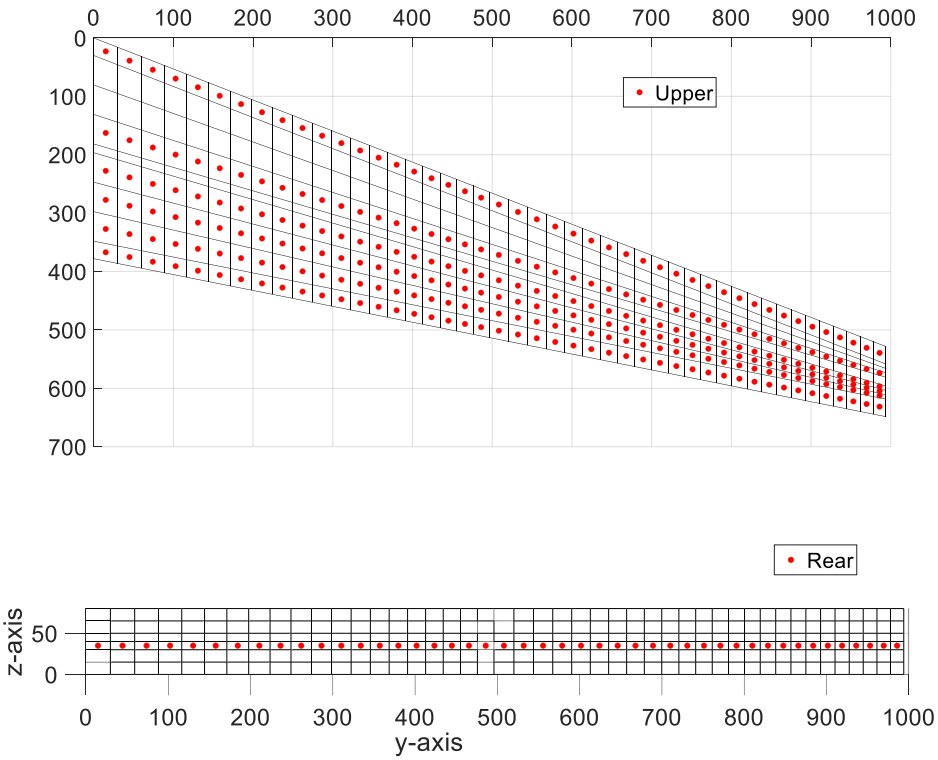

(a) two-steps method.

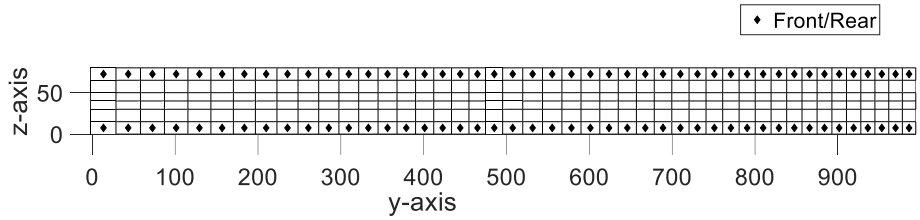

(b) iFEM

Figure 20: Optimal sensors configurations for Load case 2 - The figures show the optimal sensors configurations for the two-steps method (a) and the iFEM (b). In the legends, Upper and Lower refer to sensors located on the upper or lower panel, whereas Upper/lower refers to sensors located on both panels. Front and Rear refers to sensors that are located on the front or the rear spar, whereas Front/Rear refers to sensors located on both spars.

The configuration with only one sensing line deserves more attention. The nodal values of the forces, identified from the strains of this configuration, are reported in Table 4. In the table there are also the reference values for the actually applied forces. It is easy to observe that the nodal values are not well predicted. Nevertheless, looking at the resultant of the system of forces, R_z, it can be noticed that there is little discrepancy between the one relative to the reference load system and the one relative to the identified system. Moreover, the computation of the resultant moment along y, with respect to the center of gravity, M_y^G, gives the same result for the reference system of loads and the identified one. This results can explain the extreme accuracy of the novel shape sensing method for both the load cases, when few strain information is available and the external loads identification is not effective. The method is able to identify a system of loads that is different from the actually applied one, but it is equivalent in terms of the caused deformations. For the Load Case 2, it can be observed that the two systems of forces have totally different values of the forces, but are almost

equivalent as a system, having almost the same resultant of forces and the same resultant of moments. In the end, it seems that the method, when few inputs are available, is able to find one of the infinite systems of loads that can generate the deformed shape, whose induced strains are used as the inputs for the method.

Table 4: Load identification of Load Case 2 with only 1 sensing line - The positive directions and the identification numbers of the forces are the ones depicted in Figure 5.

	Loads	$\%ERMS_f$	R_z	M_y^G
Ref	$F_1 = F_{19} = 749N;\ F_2 = F_{18} = 1,499N;\ F_3 = F_{17} = 937N;$ $F_{4-8} = F_{12-16} = 375N;\ F_9 = F_{11} = 562N;\ F_{10} = 749N$	-	$11,993N$	$0N \cdot mm$
Rec	$F_1 = 814N;\ F_2 = 1,313N;\ F_3 = 1,832N;\ F_4 = 957N;$ $F_5 = -1,221N;\ F_6 = 367N;\ F_7 = 853N;\ F_8 = 155N;$ $F_9 = 953N;\ F_{10} = 592N;\ F_{11} = 858N;\ F_{12} = -926N;$ $F_{13} = 1,056N;\ F_{14} = 878N;\ F_{15} = -661N;\ F_{16} = -139N;$ $F_{17} = 2,276N;\ F_{18} = 726N;\ F_{19} = 1,307N$	50.10%	$11,990N$	$0N \cdot mm$

5.3.4 Effect of measurement error

In this section, the influence of measurement error for the two-steps approach is evaluated. To take into account for this errors, two cases of normally distributed errors with zero mean and a standard deviation of 1% and 5% of the nominal value are added to the strains obtained from the high-fidelity FEM analysis. The same two load cases from the previous analysis are considered and only the more representative optimal sensors configurations have been selected for this application, namely the 1 line and the 7 lines configurations for both load cases. Moreover, in order to smooth the amplification of the error due to the ill-posedness of the problem, the Tikhonov regularization has been introduced in the solution of the inverse problem formulated in Eqs. 5 and 7. For each case, the Tikhonov regularization parameter (λ) has been computed empirically, searching for the value that maximized the accuracy in the reconstruction of the external loads. In Table 5 and 6, the results of these analysis are reported for the two load cases respectively. The results, in terms of $\%ERMS_p$, $\%ERMS_f$ and $\%ERMS_w$, are presented for the reconstructions obtained with and without the use of the Tikhonov regularization. In the tables, the values of the regularization parameters, λ, are also reported.

Table 5: Effect of measurement error for **Load case 1**.

		NO regularization		Tikhonov regularization		
%Err	Sensors	$\%ERMS_p$	$\%ERMS_w$	$\%ERMS_p$	$\%ERMS_w$	λ
1%	1 line	934.6	9.9	23.1	0.5	7.0E-06
	7 lines	29478.4	13.6	15.5	0.06	8.0E-05
5%	1 line	2782.2	19.8	27.3	0.8	7.0E-05
	7 lines	247754.6	66.4	18.3	1.1	2.4E-04

Table 6: Effect of measurement error for **Load case 2**.

		NO regularization		Tikhonov regularization		
%Err	Sensors	$\%ERMS_f$	$\%ERMS_w$	$\%ERMS_f$	$\%ERMS_w$	λ
1%	1 line	21512113.2	448.7	22.1	3.5	2.0E-09
	7 lines	210209.8	32.0	23.3	0.04	3.0E-08
5%	1 line	130845922	2578.9	25.8	7.2	7.0E-09
	7 lines	4749253.5	58.5	23.5	0.2	2.0E-08

The results show that the two-step procedure is heavily influenced by the measurement error and that these errors have a strong effect on the quality of the reconstruction of the loads and consequently also on the computation of the displacement field. Even the case with 1% error gives highly inaccurate reconstructions for both load cases and for every sensors configuration. Nevertheless, it can be noticed that the introduction of the Tikhonov regularization is able to effectively reduce the inaccuracy introduced by the measurement error. In fact, the regularization allows the reduction of the errors in the reconstruction of the loads ($\%ERMS_p$,$\%ERMS_f$) from values that reach, in the best case, almost 1000%, to values that, in the worst case, are close to 27%. In addition, the quality of the reconstructed shape, obtained from the second step of the method, is even more positively influenced by the Tikhonov regularization. As a matter of fact, the deformed shape is reconstructed with impressive accuracy for all the analyzed configurations ($0.06 < \%ERMS_w < 1.2$), with the exception of the Load case 2 with only one sensing line ($\%ERMS_w > 3$). The analysis of the configuration with 7 sensing lines is reported in the following to demonstrate the above mentioned behaviors. Figure 21 shows the reconstruction of the Load case 1 when 1% error (Fig. 21a) and the 5% error (Fig. 21b) are introduced into the input strains and the Thikonov regularization is adopted. The figures, when compared with Figure 3, confirm that the method is only capable of a moderate reconstruction of the pressure distribution. On the other hand, Figure 22 demonstrates that the shape sensing, under the same test conditions, is still really accurate. Figure 23 presents the reconstruction of the nodal forces of Load case 2. In the figure, the results are reported for the 7 lines sensors configuration when 1% (Fig. 23a) and 5% (Fig. 23b) measurement errors are introduced. The resultants R_z and M_y^G, as defined in Section 5.3.3, are also reported inside the figures. The accuracy in the prediction of the single values of the nodal forces is modest and, although R_z, compared with the reference one reported in Table 4, is well predicted, the values of the resultant moment, M_y^G, are far from the reference one, especially for the 5% error configuration. Nevertheless, the derived wing tip displacements, shown in Figure 24, prove once again the good results obtained by the shape sensing step. As a consequence, it can be inferred that the magnitude of the discrepancy in the identified resultant moment is not so relevant to induce considerable effects on the deformation of the box.

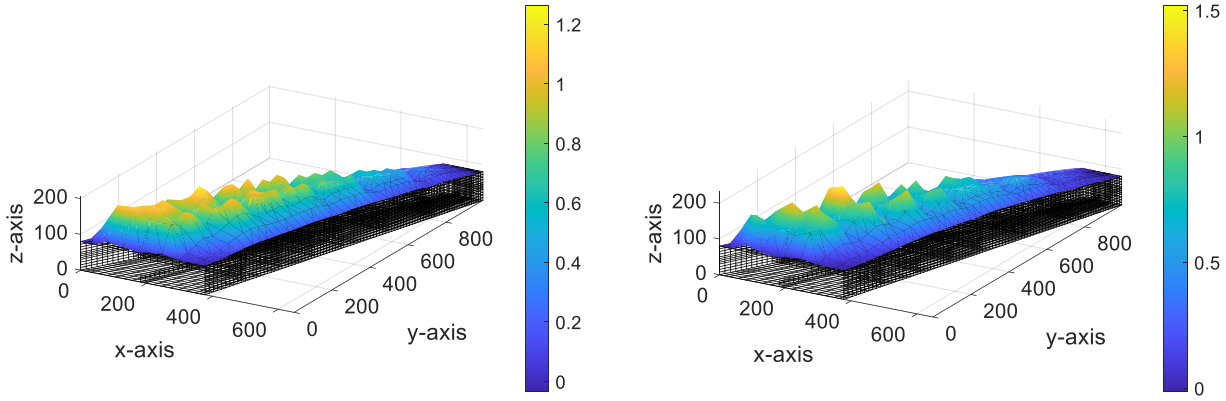

(a) 1% Error.

(b) 5% Error.

Figure 21: Pressure field reconstructions for Load Case 2 when strains are affected by a normal error of 1% (a) and 5% (b) and the Thikonov regularization is implemented. The results are showed for the 7 sensing lines configuration.

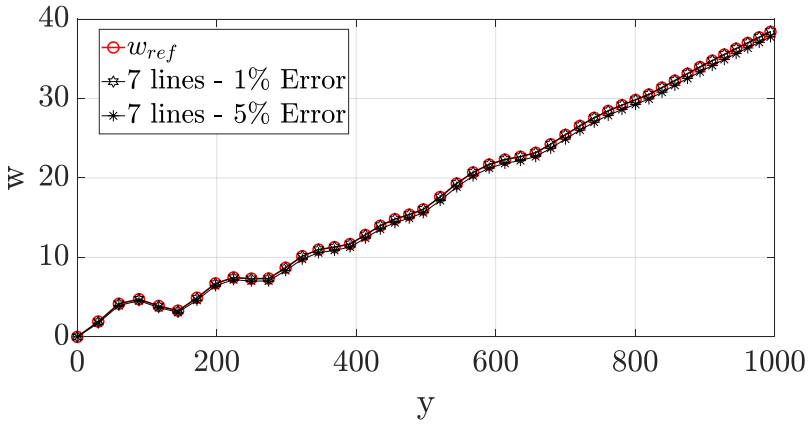

Figure 22: Vertical deflection along the wing span for Load Case 1 when strains are affected by a normal error of 1% and 5% and the Thikonov regularization is implemented. The results are showed for the 7 sensing lines configuration.

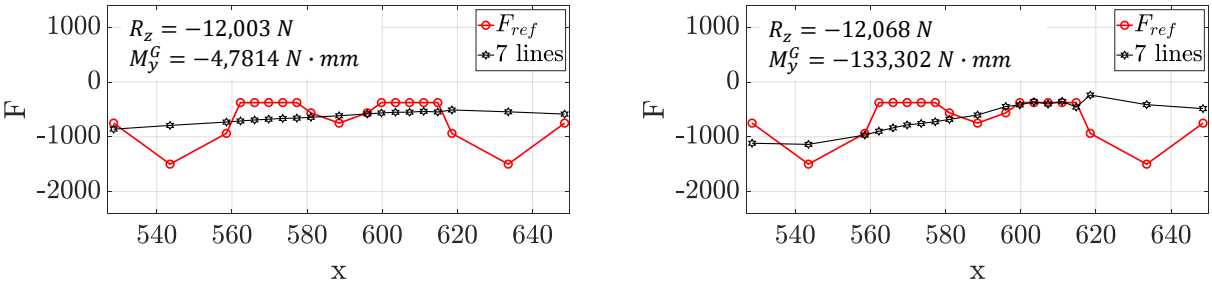

(a) 1% Error.

(b) 5% Error.

Figure 23: Nodal forces identification for Load Case 1 when strains are affected by a normal error of 1% (a) and 5% (b). The results are showed for the 7 sensing lines configuration.

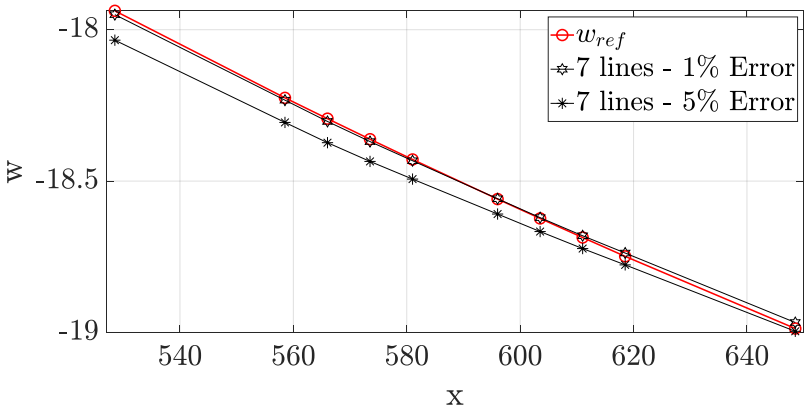

Figure 24: Vertical deflection along the wing tip chord for Load Case 2 when strains are affected by a normal error of 1% and 5%. The results are showed for the 7 sensing lines configuration.

6 Conclusions

This paper presents the study of a novel two-steps procedure designed for the simultaneous computation of the external loads and the displacement field of a structure. The first step of the method is used to identify the external loads from discrete strain measurements. The second step exploits the identified loads from the first step to perform a standard direct FEM analysis and thus derive the displacement field. The procedure has been numerically tested on an aluminum 3D swept wing box subject to two load cases, one constituted by a distributed aerodynamic pressure and one constituted by a set of concentrated forces applied at the tip section of the box. The method has been tested for different strain sensors configurations. The configurations have been inspired by the optical fiber sensing technology. Therefore, each configuration has been constituted by a varying number of sensing lines, from 1 to 10, running along the wing box span. Each sensor configuration has been optimized by selecting the best configuration of sensing lines in order to obtain the best accuracy in the external load identification. The results of the novel shape sensing technique have been compared to the ones obtained with the well established iFEM.

The external load identification has proven to be improved by the introduction of the quadrilateral elements and has shown to be accurate when a sufficient number of sensing lines is adopted. For both the load cases, a significant level of accuracy is achieved for the configurations with 7 sensing lines. The reduction in the number of sensing lines provokes a continuous loss of accuracy in the loads identification, reaching considerable values of the errors for the configuration with only 1 sensing line.

The same behavior can be observed for the shape sensing step. The reduction in the number of sensing lines obviously produces a lost of accuracy. However, in this case, the reached accuracy level is impressive and strongly more precise than the iFEM for any sensors configuration and for any load case. With only 1 sensing line the method is capable of a remarkable displacements reconstruction. The deeper analysis of this phenomena brought to light that the method, when few strain information is available, is unable to identify the actually applied external loads, but it is able to identify one of the infinite equivalent system of loads, whose action on

the structure induces the measured strain field and, consequently, the investigated displacement field.

The introduction of measurement error has a significantly negative influences on the quality of the loads identification and shape sensing. Nevertheless, in this case, the use of a regularization method, such as the Tikhonov regularization, is able to improve the accuracy of the load identification step, although reaching moderate levels of accuracy, and it allows the second step, once again, to produce remarkable reconstructions of the displacement field.

In conclusion, the proposed method is able to simultaneously identify the external loads and the displacement field of a structure when a sufficient number of discrete strains are provided to the method. When the number of strains is not sufficient or they are affected by measurement error, the two-steps procedure is still capable of remarkable results in the deformed shape reconstruction. In future works, the obtained results should be validated experimentally. Moreover, the capability of the load identification step should be tested on the reconstruction of discontinuous aerodynamic distributions, such as the ones typical of transonic wings, and on more complex and realistic pressure distributions, extended to the whole structural domain of the wing box.

Acknowledgments:
Computational resources were provided by HPC@POLITO, a project of Academic Computing within the Department of Control and Computer Engineering at the Politecnico di Torino (http://www.hpc.polito.it)

A Appendix: Pressure distribution

The pressure distribution is obtained by multiplying a third order polynomial of x and a second order polynomial of y:

$$p(x,y) = p_1(x) \cdot p_2(y) = (a_x x^3 + b_x x^2 + c_x x + d_x) \cdot (a_y y^2 + b_y y + c_y) \tag{A.1}$$

To find the coefficients of the polynomials it is necessary to impose the conditions described in Section 4.2. They can be expressed mathematically as follows. The three conditions necessary to find the three coefficients of the $p_2(y)$ polynomial are:

$$\begin{cases} p_2(y = 994) = 0 \quad p_2 \text{ equal to 0 at the tip section} \\ p_2(y = 0) = 1 \quad p_2 \text{ is equal to 1 at the root section} \\ p_{2,y}(y = 0) = 0 \quad p_2 \text{ has a maximum at the root section} \end{cases} \tag{A.2}$$

The four conditions necessary to find the four coefficients of the $p_1(x)$ polynomial are:

$$\begin{cases} p_1\left(x = \frac{528.52}{994}y\right) = 0 & p_1 \text{ equal to 0 at the leading edge} \\ p_1\left(x = \frac{270.52}{994}y + 378\right) = 0 & p_1 \text{ equal to 0 at the trailing edge} \\ p_1\left(x = \frac{618.69}{994}y + 126\right) = 1 & p_1 \text{ equal to 1 at one third of the chord} \\ p_{1,x}\left(x = \frac{618.69}{994}y + 126\right) = 0 & p_1 \text{ has a maximum at one third of the chord} \end{cases} \tag{A.3}$$

where $(x = \frac{528.52}{994}y + 378)$ is the equation of the leading edge, $(x = \frac{270.52}{994}y + 378)$ is the equation of the trailing edge and $(x = \frac{618.69}{994}y + 126)$ is the equation of locus of the points at one-third of the chords.

Since the wing box's panel is swept, the leading edge, the trailing edge and the point at one third of the chord have different x values for every y section of the wing panel. Therefore, the coefficients of the $p_1(x)$ polynomial depend on the y coordinate, as expressed in Eqs. A.3, and they have to be computed for each value of y.

References

[1] T. Nakamura, H. Igawa, and A. Kanda. Inverse identification of continuously distributed loads using strain data. *Aerospace Science and Technology*, 23(1):75 – 84, 2012, doi:https://doi.org/10.1016/j.ast.2011.06.012.

[2] A. Airoldi, G. Sala, R. Evenblij, C. Koimtzoglou, T. Loutas, G. M. Carossa, P. Mastromauro, and T. Kanakis. Load monitoring by means of optical fibres and strain gages. In P. C. Wölcken and M. Papadopoulos, editors, *Smart Intelligent Aircraft Structures (SARISTU)*, pages 433–469, Cham, 2016. Springer International Publishing. doi:10.1007/978-3-319-22413-8_20.

[3] R. Roy, M. Gherlone, and C. Surace. Damage localisation in thin plates using the inverse finite element method. In M. A. Wahab, editor, *Proceedings of the 13th International Conference on Damage Assessment of Structures*, pages 199–212, Singapore, 2020. Springer Singapore. doi:10.1007/978-981-13-8331-1_14.

[4] M. Li, A. Kefal, B. C. Cerik, and E. Oterkus. Dent damage identification in stiffened cylindrical structures using inverse finite element method. *Ocean Engineering*, 198:106944, 2020, doi:https://doi.org/10.1016/j.oceaneng.2020.106944.

[5] J. Serafini, G. Bernardini, R. Porcelli, and P. Masarati. In-flight health monitoring of helicopter blades via differential analysis. *Aerospace Science and Technology*, 88:436 – 443, 2019, doi:https://doi.org/10.1016/j.ast.2019.03.039.

[6] T. de Souza Siqueira Versiani, F. J. Silvestre, A. B. Guimarães Neto, D. A. Rade, R. G. Annes da Silva, M. V. Donadon, R. M. Bertolin, and G. C. Silva. Gust load alleviation in a flexible smart idealized wing.

Aerospace Science and Technology, 86:762 – 774, 2019, doi:https://doi.org/10.1016/j.ast.2019.01.058.

[7] S. Barbarino, O. Bilgen, R. M. Ajaj, M. I. Friswell, and D. J. Inman. A review of morphing aircraft. *Journal of Intelligent Material Systems and Structures*, 22(9):823–877, 2011, doi:10.1177/1045389X11414084.

[8] B. J. Soller, D. K. Gifford, M. S. Wolfe, and M. E. Froggatt. High resolution optical frequency domain reflectometry for characterization of components and assemblies. *Opt. Express*, 13(2):666–674, Jan 2005, doi:10.1364/OPEX.13.000666.

[9] R. Di Sante. Fibre optic sensors for structural health monitoring of aircraft composite structures: Recent advances and applications. *Sensors*, 15(8):18666–18713, 2015, doi:10.3390/s150818666.

[10] S. Shkarayev, R. Krashanitsa, and A. Tessler. An inverse interpolation method utilizing in-flight strain measurements for determining loads and structural response of aerospace vehicles. In *Proc. Third Int. Workshop on Structural Health Monitoring*. Stanford, 2001.

[11] C. Coates, P. Thamburaj, and C. Kim. An inverse method for selection of fourier coefficients for flight load identification. In *46th AIAA/ASME/ASCE/AHS/ASC Structures, Structural Dynamics and Materials Conference*. Austin, 2005, doi:10.2514/6.2005-2183.

[12] C. W. Coates and P. Thamburaj. Inverse method using finite strain measurements to determine flight load distribution functions. *Journal of Aircraft*, 45(2):366–370, 2008, doi:10.2514/1.21905.

[13] A. Airoldi, L. Marelli, P. Bettini, G. Sala, and A. Apicella. Strain field reconstruction on composite spars based on the identification of equivalent load conditions. In J. P. Lynch, editor, *Sensors and Smart Structures Technologies for Civil, Mechanical, and Aerospace Systems 2017*, volume 10168, pages 207 – 226. International Society for Optics and Photonics, SPIE, 2017. doi:10.1117/12.2260161.

[14] D. Wada and Y. Sugimoto. Inverse analysis of aerodynamic loads from strain information using structural models and neural networks. In J. P. Lynch, editor, *Sensors and Smart Structures Technologies for Civil, Mechanical, and Aerospace Systems 2017*, volume 10168, pages 227 – 233. International Society for Optics and Photonics, SPIE, 2017. doi:10.1117/12.2258583.

[15] P. M. Trivailo and C. L. Carn. The inverse determination of aerodynamic loading from structural response data using neural networks. *Inverse Problems in Science and Engineering*, 14(4):379–395, 2006, doi:10.1080/17415970600573692.

[16] S. B. Cooper and D. DiMaio. Static load estimation using artificial neural network: Application on a wing rib. *Advances in Engineering Software*, 125:113 – 125, 2018, doi:10.1016/j.advengsoft.2018.01.007.

[17] W. L. Ko, W. L. Richards, and V. T. Fleischer. Displacement theories for in-flight deformed shape predictions of aerospace structures. Report NASA/TP-2007-214612, NASA Dryden Flight Research Center; Edwards, CA, United States, 2007.

[18] C. Pak. Wing shape sensing from measured strain. *AIAA Journal*, 54(3):1068–1077, 2016. doi:10.2514/1.J053986.

[19] G. Ding, S. Yue, S. Zhang, and W. Song. Strain - deformation reconstruction of cfrp laminates based on ko displacement theory. *Nondestructive Testing and Evaluation*, 0(0):1–13, 2020. doi:10.1080/10589759.2019.1707200.

[20] G. C. Foss and E. D. Haugse. Using Modal Test Results to Develop Strain to Displacement Transformations. In *Proceedings of the 13th International Modal Analysis Conference*. Nashville, 1995.

[21] P. Bogert, E. Haugse, and R. Gehrki. Structural shape identification from experimental strains using a modal transformation technique. In *44th AIAA/ASME/ASCE/AHS/ASC Structures, Structural Dynamics, and Materials Conference*. Norfolk, 2012. doi:10.2514/6.2003-1626.

[22] M. Freydin, M. K. Rattner, D. E. Raveh, I. Kressel, R. Davidi, and M. Tur. Fiber-optics-based aeroelastic shape sensing. *AIAA Journal*, 57(12):5094–5103, 2019. doi:10.2514/1.J057944.

[23] M. Gherlone, P. Cerracchio, and M. Mattone. Shape sensing methods: Review and experimental comparison on a wing-shaped plate. *Progress in Aerospace Sciences*, 99:14 – 26, 2018, doi:10.1016/j.paerosci.2018.04.001.

[24] A. Tessler and J. L. Spangler. Deformed shape calculation of a full-scale wing using fiber optic strain data from a ground loads test. Report NASA/TM-2003-212445, NASA Langley Research Center, Hampton, VA, United States, 2003.

[25] M. Gherlone, P. Cerracchio, M. Mattone, M. D. Sciuva, and A. Tessler. Shape sensing of 3d frame structures using an inverse finite element method. *International Journal of Solids and Structures*, 49(22):3100 – 3112, 2012, doi:10.1016/j.ijsolstr.2012.06.009.

[26] M. Gherlone, P. Cerracchio, M. Mattone, M. D. Sciuva, and A. Tessler. An inverse finite element method for beam shape sensing: theoretical framework and experimental validation. *Smart Materials and Structures*, 23(4):045027, 2014, doi:10.1088/0964-1726/23/4/045027.

[27] P. Cerracchio, M. Gherlone, and A. Tessler. Real-time displacement monitoring of a composite stiffened panel subjected to mechanical and thermal loads. *Meccanica*, 50:2487–2496, 2015, doi:10.1007/s11012-015-0146-8.

[28] E. J. Miller, R. Manalo, and A. Tessler. Full-field reconstruction of structural defor- mations and loads from measured strain data on a wing using the inverse finite element method. Report NASA/TM-2016-219407, NASA Dryden Flight Research Center; Edwards, CA United States, 2016.

[29] A. Kefal, E. Oterkus, A. Tessler, and J. L. Spangler. A quadrilateral inverse-shell element with drilling degrees of freedom for shape sensing and structural health monitoring. *Engineering Science and Technology, an International Journal*, 19(3):1299 – 1313, 2016, doi:10.1016/j.jestch.2016.03.006.

[30] A. Kefal and E. Oterkus. Displacement and stress monitoring of a panamax containership using inverse finite element method. *Ocean Engineering*, 119:16 – 29, 2016, doi:10.1016/j.oceaneng.2016.04.025.

[31] A. Kefal and E. Oterkus. Isogeometric ifem analysis of thin shell structures. *Sensors*, 20(9), 2020, doi:10.3390/s20092685.

[32] U. Papa, S. Russo, A. Lamboglia, G. D. Core, and G. Iannuzzo. Health structure monitoring for the design of an innovative uas fixed wing through inverse finite element method (ifem). *Aerospace Science and Technology*, 69:439 – 448, 2017, doi:10.1016/j.ast.2017.07.005.

[33] M. Esposito and M. Gherlone. Composite wing box deformed-shape reconstruction based on measured strains: Optimization and comparison of existing approaches. *Aerospace Science and Technology*, 99:105758, 2020, doi:10.1016/j.ast.2020.105758.

[34] E. Turco. Load distribution modelling for pin-jointed trusses by an inverse approach. *Computer Methods in Applied Mechanics and Engineering*, 165(1):291 – 306, 1998, doi:10.1016/S0045-7825(98)80013-3.

[35] R. Cook. Four-node 'flat' shell element: Drilling degrees of freedom, membrane-bending coupling, warped geometry, and behavior. *Computers & Structures*, 50(4):549 – 555, 1994, doi:10.1016/0045-7949(94)90025-6.

[36] C. Hua. An inverse transformation for quadrilateral isoparametric elements: Analysis and application. *Finite Elements in Analysis and Design*, 7(2):159 – 166, 1990, doi:https://doi.org/10.1016/0168-874X(90)90007-2.